Supporting information

For

Eliminating water molecules through tailored crystal orientation to enhance the lithium storage capacity of iron oxalate

1. Texture coefficient calculations

The texture coefficients ($T_{(hkl)}$) were calculated using the following equation **[1].** Additionally, the Rietveld refinement was conducted using the GSAS software (http://www.ccp14.ac.uk/solution/gsas/) **[2, 3]**.

$$T_{(hkl)} = \frac{I_{(hkl)}/I_{0(hkl)}}{(1/n \times \sum I_{(hkl)}/I_{0(hkl)})}$$

Where $I(hkl)$ and $I_0(hkl)$ represent the measured and standard peak intensities of the (hkl) crystallographic plane, respectively. The parameter n denotes the total number of crystallographic planes considered.

2. Analysis of DRT

The DRT transition was performed using the DRT Tools for MATLAB platform, developed by the Ciucci Group (https://ciucci.org/project/drt/) **[4]**. The computation of the DRT is based on Tikhonov regularization with continuous function discretization. The EIS data selected for DRT calculation is from the "Combined Re-Im Data." A Gaussian function is used as the discretization function, and the regularization derivative employed in the penalty is the first-order derivative. The regularization parameter (λ) is set to 1000 to achieve a smoother DRT profile. The total number of samples is 10,000, and the shape control of the Radial Basis Function is configured with a "FWHM coefficient" of 0.5.

3. The density functional theory calculations

Density Functional Theory (DFT) calculations were performed using the CASTEP package with the Generalized Gradient Approximation (GGA) of Perdew-Burke-Ernzerhof (PBE). Surfaces were cleaved from an optimized bulk structure. The

sectioning was based on the conventional cell, followed by broadening the cell and introducing a 15 Å vacuum layer. The surface dimensions were defined as (200) U×V=3×2, (002) U×V=2×4, and (202) U×V=1×4. The surface energy and binding energy were calculated using the total energies of H_2O and CH_3CH_2OH adsorbed on α-$FeC_2O_4 \cdot 2H_2O$ (200), (002), and (202) surfaces to determine the preferred planes for H_2O and CH_3CH_2OH adsorption during synthesis.

$$\gamma = \frac{1}{2A}[E_{slab} - nE_{bulk}] \quad (1)$$

$$E_{bind} = E_{X-slab} - E_{X-DX} - E_x \quad (2)$$

where E_{unit} is the total energy of a pure unit, A surface area unit is eV/Å^2. E_{x-slab} and E_{x-Dx} are the total energies for X (the H_2O and CH_3CH_2OH) terminated slabs, respectively**[5, 6, 7, 8, 9]**.

In the calculations, an optimized conventional cell comprising 52 atoms was used to construct surfaces with atomic numbers that are integer multiples of 52, resulting in a total of four layers. The lower two layers were fixed, while the upper two layers were allowed to relax. Specifically, the (202) surface contained 156 atoms with an area of 116.7558 Å^2, the (002) surface contained 52 atoms with an area of 35.8878 Å^2, and the (200) surface contained 104 atoms with an area of 54.8881 Å^2. The Complete LST/QST method was employed to analyze the crystal water removal processes from the (202), (002), and (200) crystal faces. Given that the O-H bond in water molecules is more difficult to break than the Fe-O coordination bond between Fe and water molecules during dehydration, the water molecules were treated as a single entity, and the transition state was identified accordingly. The surface dimensions were set to U×V=2×1 for the (202) and (200) faces, with a thickness of two layers. For the (002) face, U×V=2×2 was used. The transition state search was performed after the geometric optimization of the reactants and products, with the dehydrated water molecules positioned at a distance of 6 Å above the initial water molecules. The RMS convergence criterion was set to 0.25 eV/Å **[10, 11].**

4. The Li^+ ions diffusion coefficient based on the following equation

S1[12, 13].

$$Z_{re} = R_s + R_{st+ct} + \sigma\omega^{-0.5}$$

$$D_{Li+} = (R^2T^2)/(2A^2F^4\sigma^2C^2)$$

Where ω represents the angular frequency in the low-frequency region; R=8.314J $mol^{-1}K^{-1}$ is the gas constant, T=298.15 K is the temperature, A=1.5386cm^2 is the electrode surface area, F=96500$Cmol^{-1}$ is Faraday's constant, and C=1$molL^{-1}$ represents the molar concentration of Li^+ ions. It is assumed that the concentration of Li^+ ions inside the material is uniform.

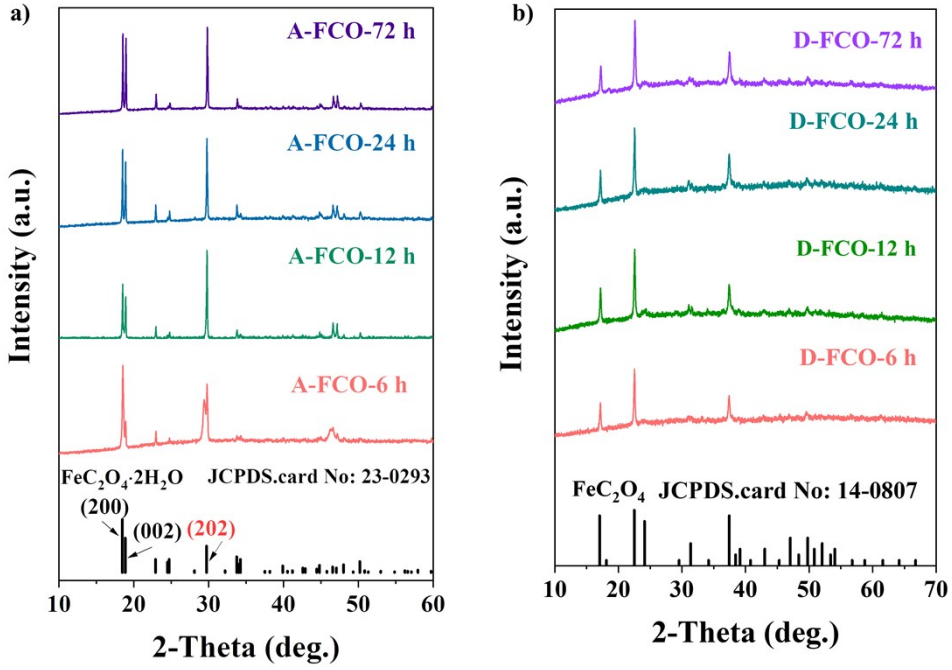

Figure S1. XRD patterns of iron oxalate prepared at different reaction times. a) Dihydrate iron oxalate, b) Anhydrous iron oxalate.

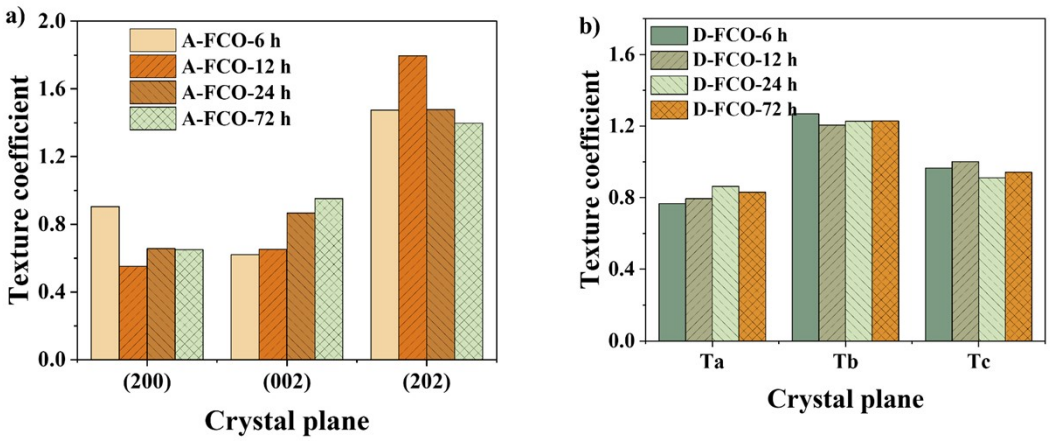

Figure S2. Texture coefficients of iron oxalate prepared at different reaction times. a) Dihydrate iron oxalate, b) Anhydrous iron oxalate.

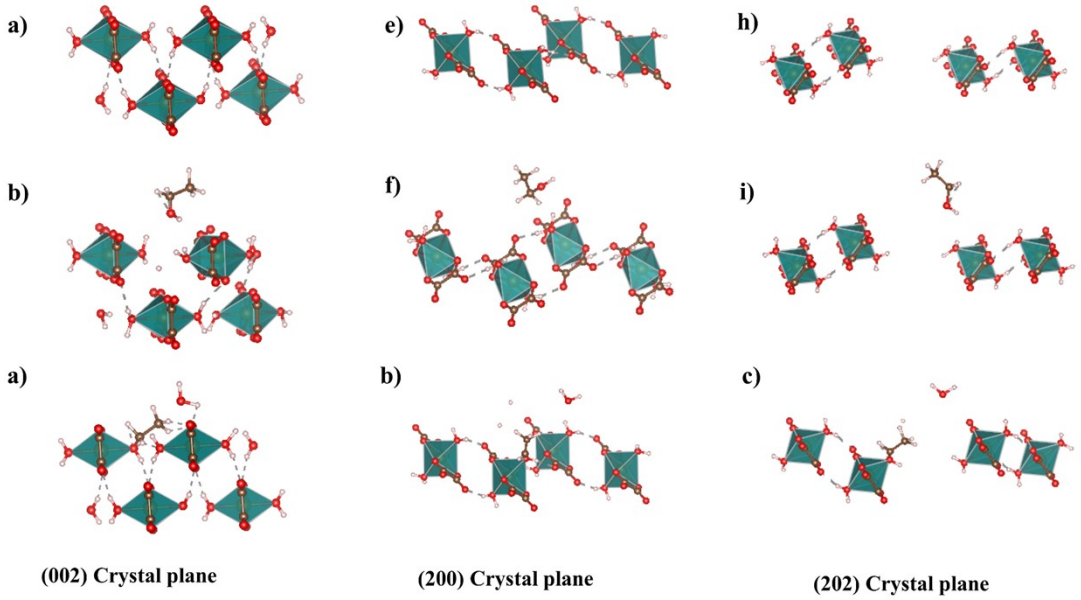

Figure S3. Structural models of terminated (200), (002), and (202) surfaces of $FeC_2O_4 \cdot 2H_2O$, illustrating the competition between the hydroxyl oxygen in ethanol and the oxygen in water molecules for coordination with Fe. a-c) (002), e-g) (200), h-j) (202).

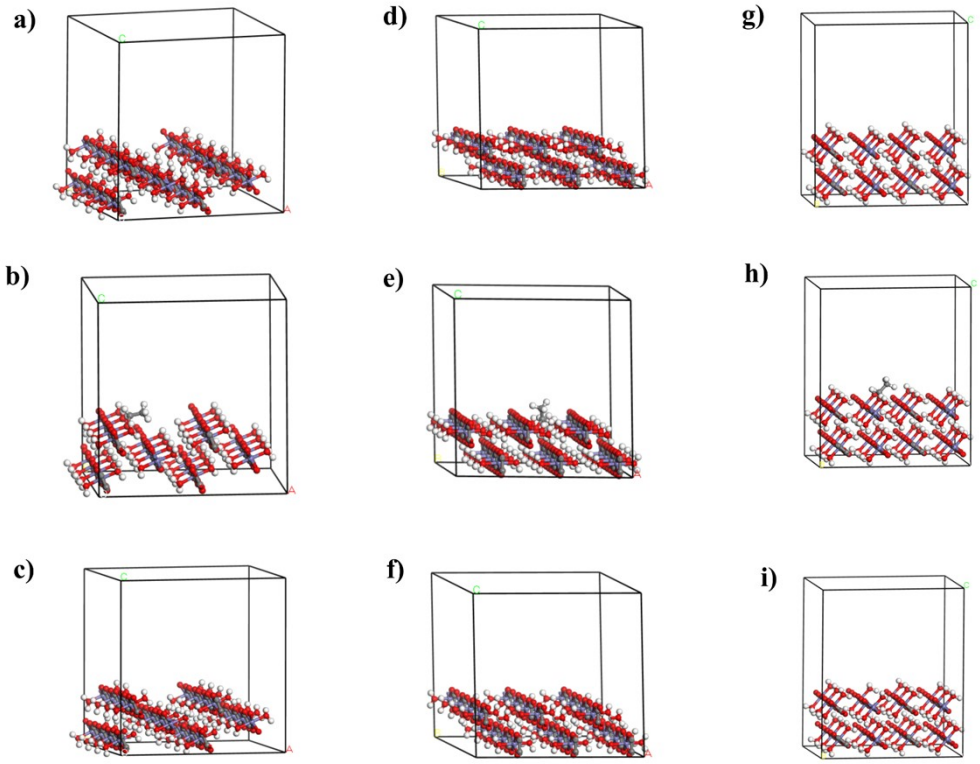

Figure S4. Calculated models of terminated (202), (002), and (200) surfaces, showing the coordination of hydroxyl oxygen in ethanol and the oxygen in water molecules with Fe. a-c) (202), e-g) (002), h-j) (200).

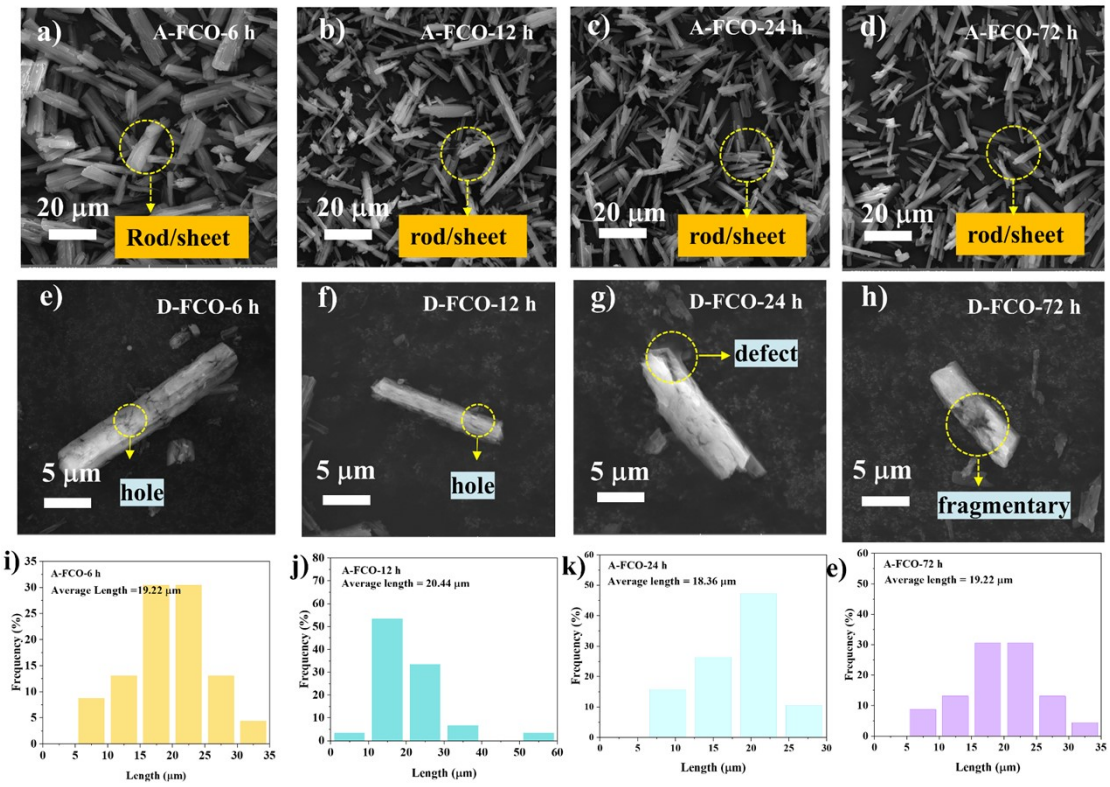

Figure S5. SEM images of iron oxalate prepared at different reaction times: dihydrate iron oxalate after a) 6 h, b) 12 h, c) 24 h, d) 72 h; after heating: e) 6 h, f) 12 h, g) 24 h, h) 72 h.

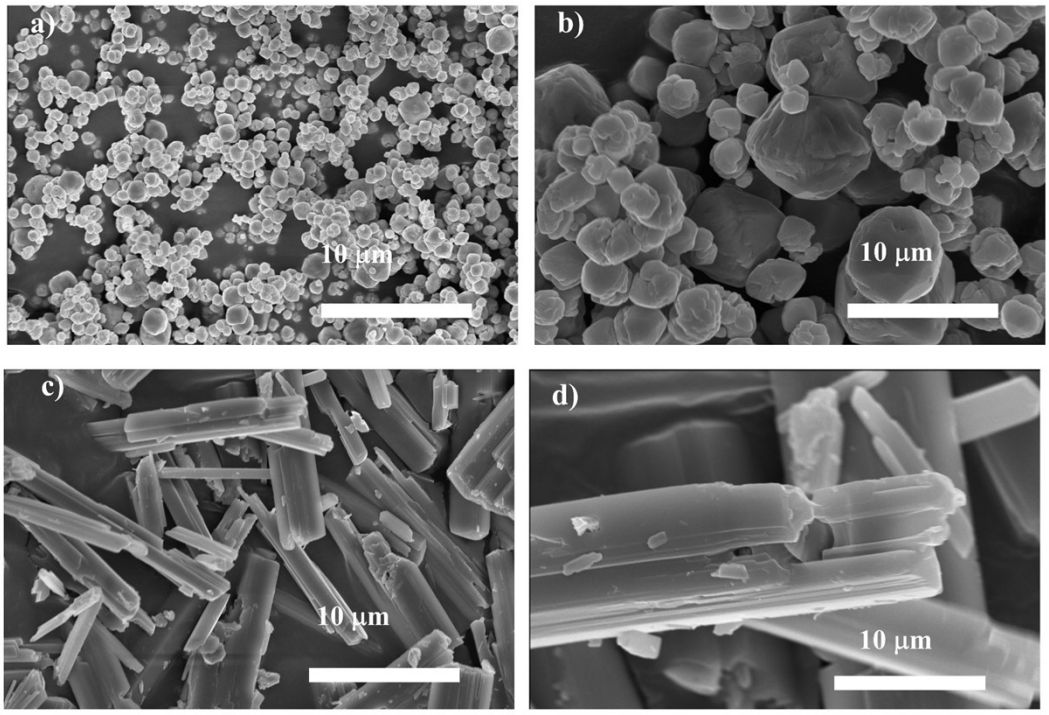

Figure S6. a) and b) SEM images of precursor materials; c) and d) precipitation particle diagrams after 3 hours.

Table 1: Detailed Assignment of CV Peaks for $FeC_2O_4 \cdot 2H_2O$

Cycle	Discharge	Charge
1cycle	0.62 V: Reduction of Fe^{2+} to Fe and decomposition of the electrolyte. 0 V: Interfacial capacitive effect between Fe (e^-) and Li^+.	0 V: Interfacial capacitive effect between Fe (e^-) and Li^+. 1.07V, $Fe \rightarrow Fe^{2+}$
2cycle	1.76 V and 1.07 V: Reactions between the electrolyte and water molecules; The reduction peak near 0.43 V corresponds to the reduction of Fe^{2+} to Fe; 0 V: Interfacial capacitive effect between Fe (e^-) and Li^+.	0 V: Interfacial capacitive effect between Fe (e^-) and Li^+; 1.07V, $Fe \rightarrow Fe^{2+}$ ；
3cycle	The reduction peak near 0.43 V corresponds to the reduction of Fe^{2+} to Fe; 0 V: Interfacial capacitive effect between Fe (e^-) and Li^+.	1.07V, $Fe \rightarrow Fe^{2+}$

Table 2: Detailed Assignment of CV Peaks for FeC_2O_4

Cycle	Discharge	Charge
1cycle	The reduction peak at 1.13 V corresponds to the reduction of Fe^{2+} to Fe and the decomposition of the electrolyte. The reduction peak at 0.57 V corresponds to the reduction of oxalate groups [14]. The reduction peak near 0 V corresponds to the interfacial capacitive effect between Fe (e^-) and Li^+ as well as the further reduction of oxalate groups.	The oxidation peak near 0 V corresponds to the interfacial capacitive effect between Fe (e^-) and Li^+. The oxidation peak at 1.20 V corresponds to the oxidation reaction of Li-C-O compounds to oxalate groups [14]. The peak at 1.53 V is attributed to the oxidation of Fe to Fe^{2+}; The oxidation peak at 2.37 V is attributed to the oxidation of Fe^{2+} to Fe^{3+}.
2cycle	The reduction peak at 1.40 V is attributed to the reduction of Fe^{3+} to Fe^{2+}; The reduction peak at 1.04 V is attributed to the reduction of Fe^{2+} to elemental Fe; The oxidation peak near 0 V corresponds to the reduction of oxalate groups and the interfacial capacitive effect between Fe (e^-) and Li^+.	The oxidation peak near 0 V corresponds to the interfacial capacitive effect between Fe (e^-) and Li^+; The oxidation peak at 1.53 V corresponds to the oxidation reaction of Li-C-O compounds to oxalate groups; The oxidation peak at 1.88 V corresponds to the oxidation reaction of Fe to Fe^{2+}.
3cycle	The broad reduction peak at 0.83 V is attributed to the conversion of Fe^{2+} to elemental iron and the reduction of oxalate groups; The oxidation peak near 0 V corresponds to the further reduction of oxalate groups and the interfacial capacitive effect between Fe (e^-) and Li^+.	The oxidation peak near 0 V corresponds to the interfacial capacitive effect between Fe (e^-) and Li^+; The oxidation peak at 1.53 V corresponds to the oxidation reaction of Li-C-O compounds to oxalate groups; The oxidation peak at 1.88 V corresponds to the oxidation reaction of Fe to Fe^{2+}.

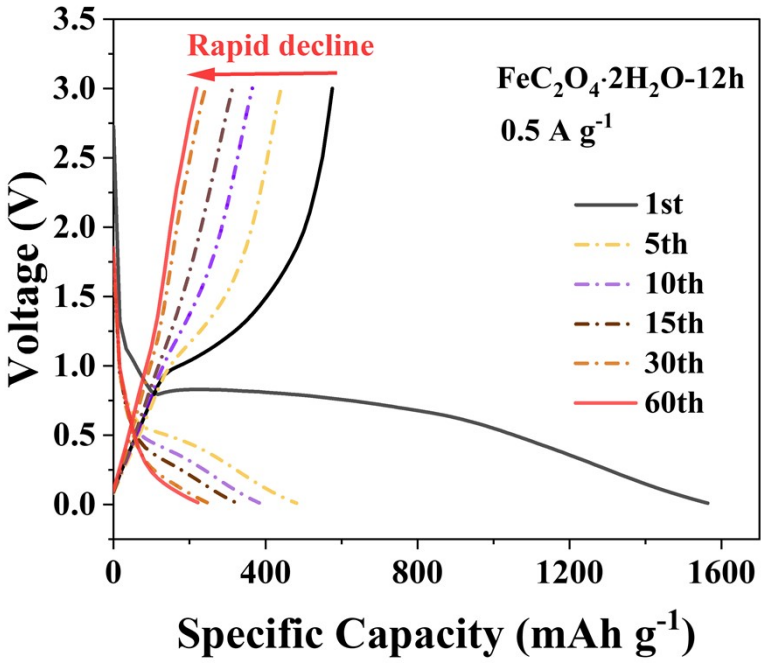

Figure S7. Galvanostatic charge-discharge curve for $FeC_2O_4 \cdot 2H_2O$-12 h at a current rate of 0.5 A g^{-1}.

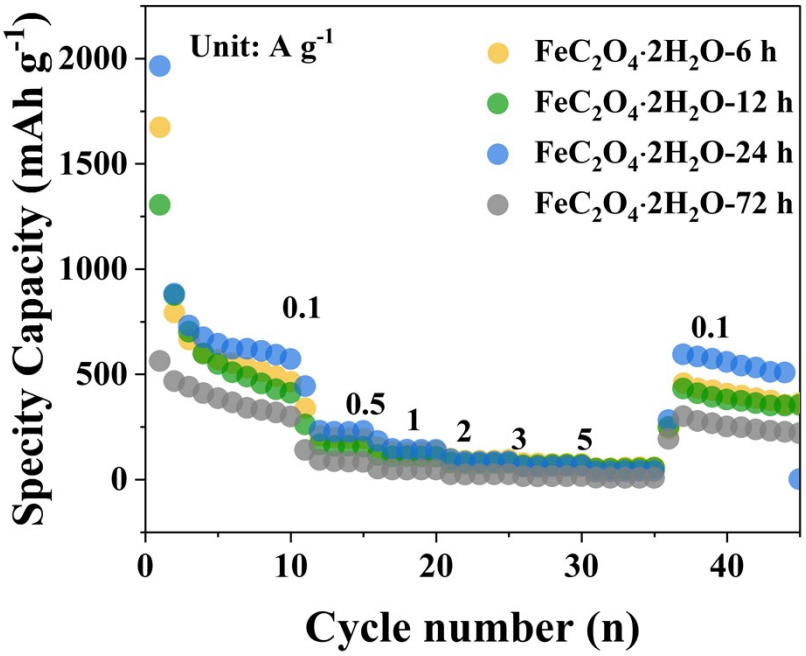

Figure S8. The rate performance for $FeC_2O_4·2H_2O$-12 h.

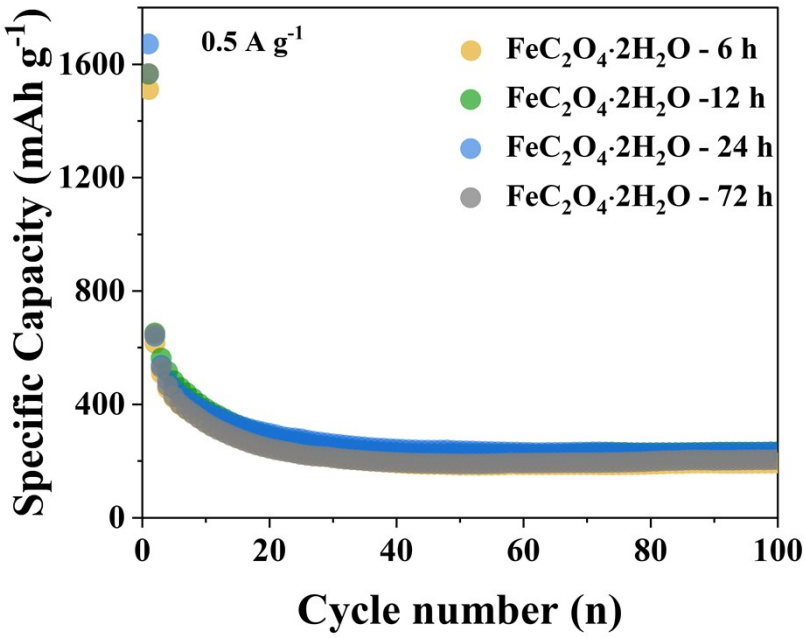

Figure S9. The rate performance for $FeC_2O_4 \cdot 2H_2O$-12 h at 0.5A g^{-1}.

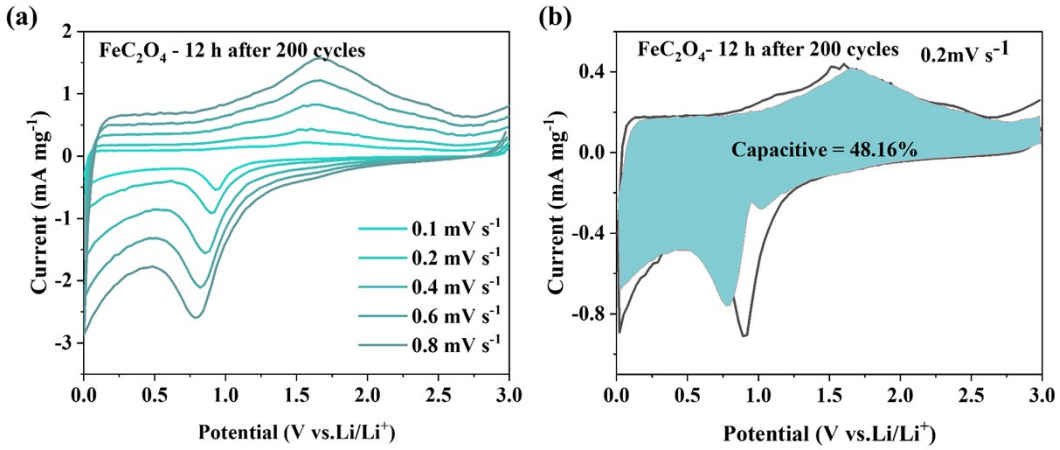

Figure S10. Capacitance contribution of FeC_2O_4-12 h. (a) Cyclic voltammetry at various sweep rates. (b) Capacitive (blue region) and diffusion-controlled (white region) contributions at 0.2 mV/s.

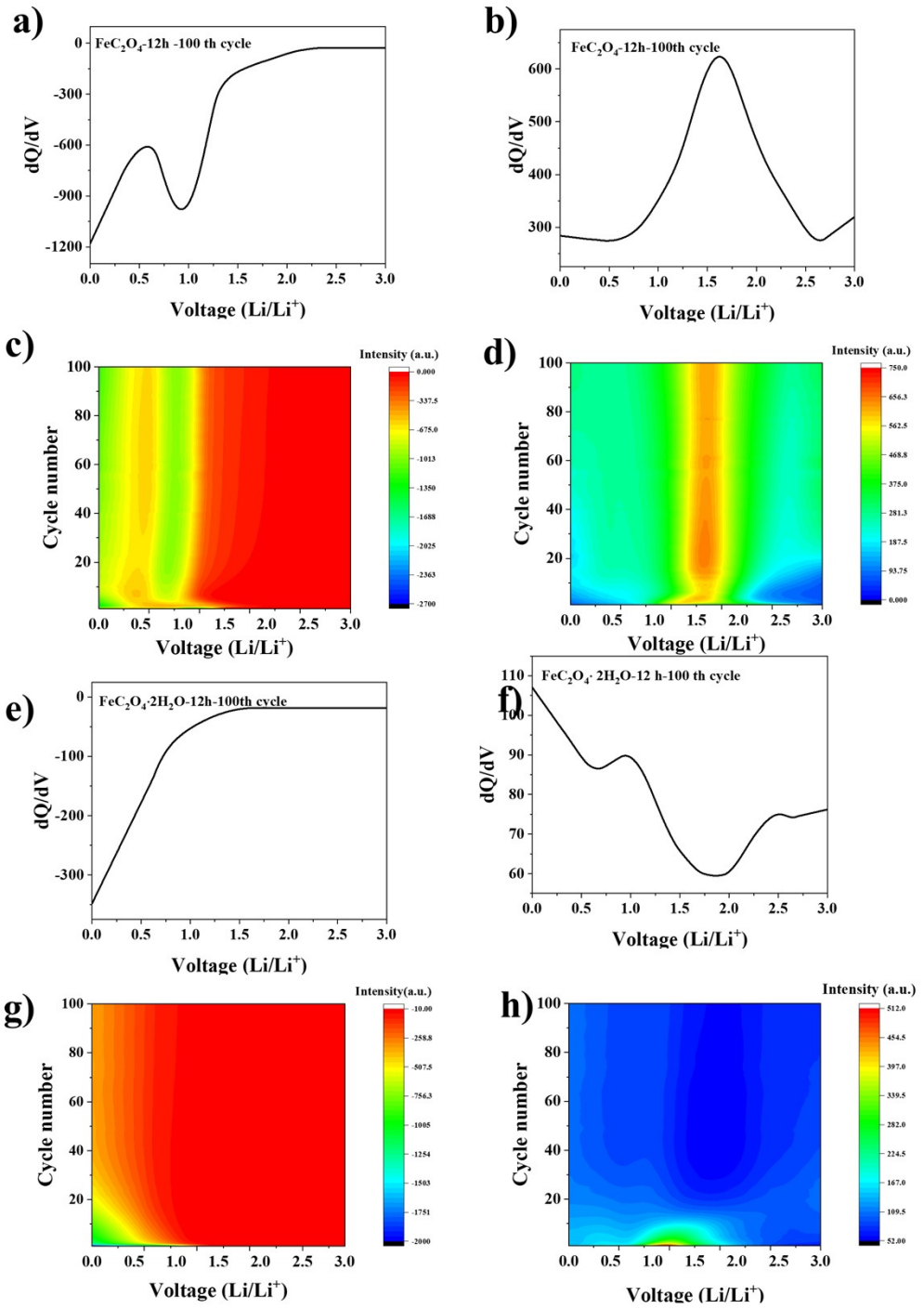

Figure S11. Curves and plots of dQ/dV for electrode materials. (a-d) FeC_2O_4; (e-f) $FeC_2O_4 \cdot 2H_2O$.

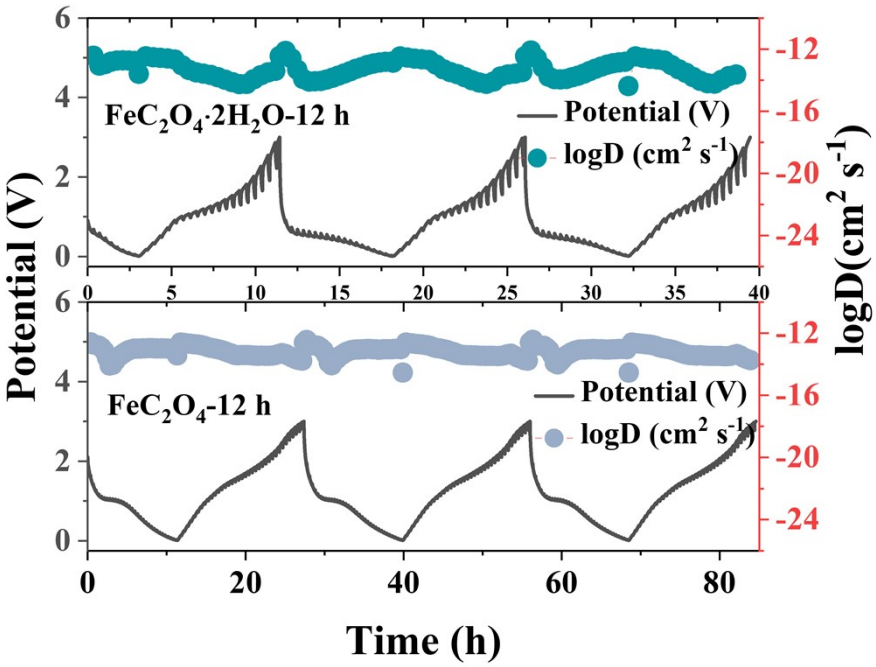

Figure S12. Galvanostatic intermittent titration technique (GITT) curve of the electrode material.

As shown in Figure S12, the FeC_2O_4 electrode exhibited a more stable lithium-ion diffusion coefficient compared to $FeC_2O_4 \cdot 2H_2O$.

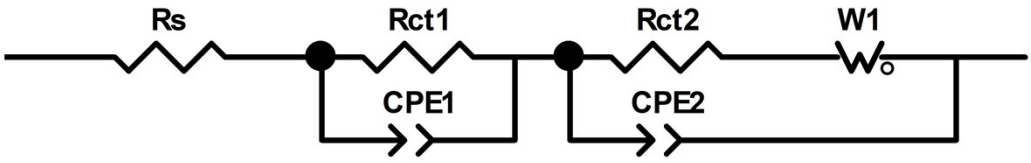

Figure S 13. The equivalent circuit diagram for the Figure 4f

Table 3. The fitting results of the equivalent circuit diagram for Figure 4f.

Sample	Rct1/Ω	Rct2/Ω
FeC_2O_4-6 h	25.01	19.01
FeC_2O_4-12 h	52.42	3.15
FeC_2O_4-24 h	29.81	9.96
FeC_2O_4-72 h	22.05	29.63

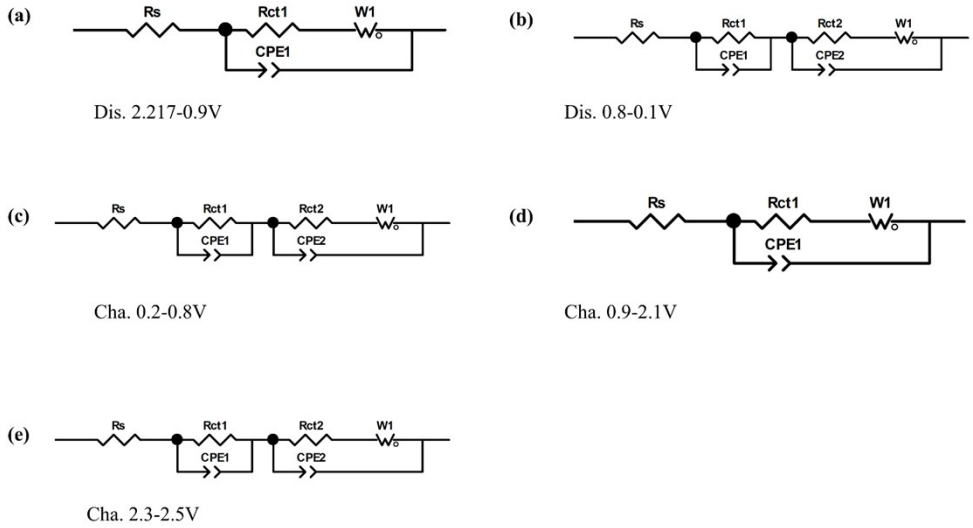

Figure S 14. The equivalent circuit diagram for the Figure 5a

Table 4. The fitting results of the equivalent circuit diagram for Figure 5a

FeC_2O_4-Dis.				FeC_2O_4-Cha.			
Voltage/V	Rct1/Ω	Rct2/Ω	Rct1+Rct2	Voltage/V	Rct1/Ω	Rct2/Ω	Rct1+Rct2
2.217	115	/	115	0.2	170.9	119.8	290.7
2.0	123.5	/	123.5	0.3	158.1	109.3	267.4
1.5	135.3	/	135.3	0.4	152.5	105.1	257.6
1.2	174.9	/	174.9	0.5	146.1	99.37	245.47
1.0	186.1	/	186.1	0.6	138.1	89.06	227.16
0.9	201.1	/	201.1	0.7	132.6	82.54	215.14
0.8	184.8	80.05	264.85	0.8	131.5	74.57	206.07
0.7	179.8	99.77	279.57	0.9	119.5	/	119.5
0.6	177.1	110.4	287.5	1.0	115.9	/	115.9
0.5	181.1	115.3	296.4	1.2	63.24	/	63.24
0.4	183.5	120.5	304	1.3	61.44	/	61.44
0.3	181.4	122.4	303.8	1.4	64.35	/	64.35
0.2	179.8	125.3	305.1	1.5	65.08	/	65.08
0.1	175.5	124.6	300.1	1.6	65.98	/	65.98
				1.7	67.9	/	67.9
				1.8	68.81	/	68.81
				1.9	69.62	/	69.62
				2.0	72.46	/	72.46
				2.1	72.96	/	72.96
				2.3	59.52	94.75	154.27
				2.5	61.8	375.7	437.5

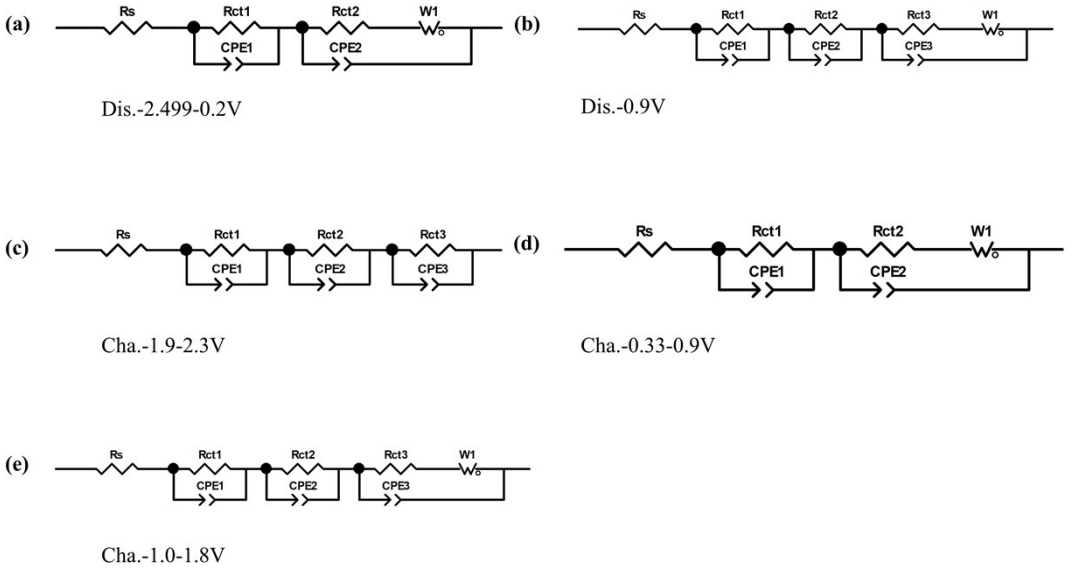

Figure S15. The equivalent circuit diagram for the Figure 5c

Table 5. The fitting results of the equivalent circuit diagram for Figure 5c

$FeC_2O_4·2H_2O$-Dis.				$FeC_2O_4·2H_2O$-Cha.			
Voltage/V	Rct1/Ω	Rct2/Ω	Rct3/Ω	Voltage/V	Rct1/Ω	Rct2/Ω	Rct3
2.449	41.37	393.5	/	0.33	422.1	79.91	/
2.2	41.74	376.6	/	0.4	38.28	444.5	/
2.0	30.79	374.8	/	0.5	32.55	422.4	/
1.5	39.49	428.1	/	0.6	34.5	315.6	/
1.2	39.7	453.3	/	0.7	38.3	248.2	/
0.9	40.36	526.4	428.5	0.8	44.3	203.8	/
0.8	34.53	530.3	/	0.9	34.77	163.9	/
0.7	26.37	609.4	/	1.0	16.08	133.8	5.325
0.5	33.03	292	/	1.2	12.76	87.91	43.74
0.4	35.91	293.3	/	1.3	15.87	78.07	53.75
0.3	44.31	318.6	/	1.4	17.83	75.37	94.46
0.2	47.47	356	/	1.5	17.48	77.66	203
				1.6	17.51	79.43	665
				1.7	17.84	80.78	2077
				1.8	18.08	82.61	3819
				1.9	24.45	74.13	10464
				2.0	18.7	86.25	14226
				2.1	18.79	89.09	22923
				2.3	19	88.9	43584

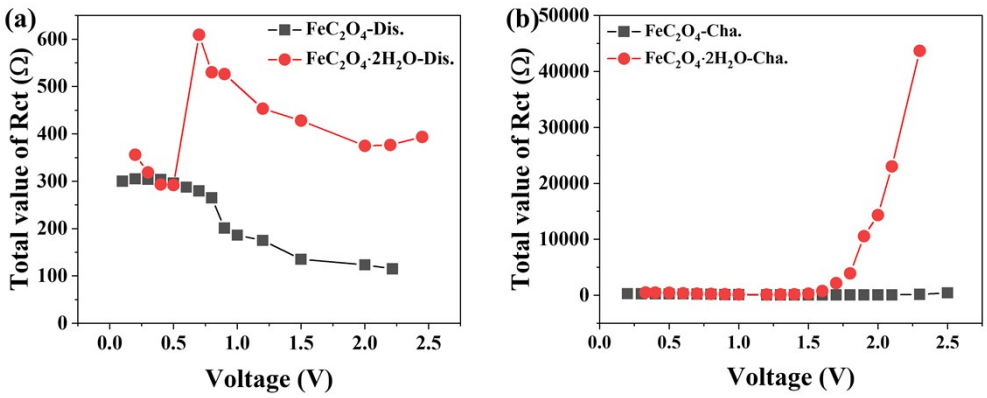

Figure S16. The charge transfer resistance (Rct) between Figure 5a and Figure 5c.

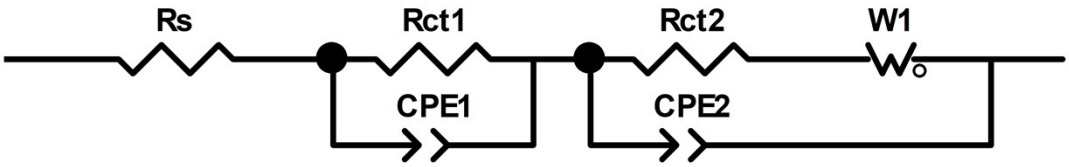

Figure S 17. The equivalent circuit diagram for the Figure 5g

Table 6. The fitting results of the equivalent circuit diagram for Figure 5g

Sample	Rct1/Ω	Rct2/Ω
FeC_2O_4	56.78	50.42
$FeC_2O_4 \cdot 2H_2O$	26.24	9.922

The potentiostatic technique:

Since the rate of electrocrystallization of new phases is a strong function of overpotential and directly reflected by current transients, potentiostatic technique was employed to probe the kinetics of SEI nucleation and growth **(Figure S18-19) [15]**. When the FeC_2O_4 electrode is maintained below the equilibrium potential for SEI formation, it first undergoes an incubation period characterized by a decrease in current, due to the stochastic clustering of minuscule SEI nuclei. Subsequently, these discrete SEI nuclei gradually enlarge and coalesce on the electrode surface, resulting in a unimodal current-time transient. In this manuscript, there are significant differences in the electrochemical performance of iron oxalate before and after the removal of crystallization water, particularly in the impedance spectra that are sensitive to the evolution of interfacial electrode information. Therefore, we employed constant voltage techniques to investigate the impact of crystallization water on the nucleation and growth of the solid-electrolyte interphase (SEI) layer on the electrode surface. To facilitate comparison with four classical nucleation models (Equation 1-4), the current-time data were normalized by the peak current (Im) and the corresponding time (tm) (**Figure 5 and Figure S18-19**). The equations for 2DI and 2DP describe two-dimensional lateral growth of cylindrical nuclei, while 3DI and 3DP model planar diffusion-controlled three-dimensional growth of hemispherical nuclei **[16].** In this context, the two-dimensional (2D) nucleation and growth mode of the solid-electrolyte interphase (SEI) layer is more conducive to the formation of a dense and fully-coated SEI layer, whereas the three-dimensional (3D) mode suggests a tendency for the SEI layer to develop a loose and porous structure.

$$j/j_m = (t/t_m)exp\{1/2[1-(t/t_m)^2]\} \quad \text{2DI} \tag{1}$$

$$j/j_m = (t/t_m)^2 exp\{2/3[1-(t/t_m)^3]\} \quad \text{2DP} \tag{2}$$

$$j/j_m = (1.9542t/t_m)^{1/2}\{1-exp[1.2564t/t_m]\} \quad \text{3DI} \tag{3}$$

$$j/j_m = (1.2254t/t_m)^{1/2}\{1-exp[2.3367(t/t_m)^2]\} \quad \text{3DP} \tag{4}$$

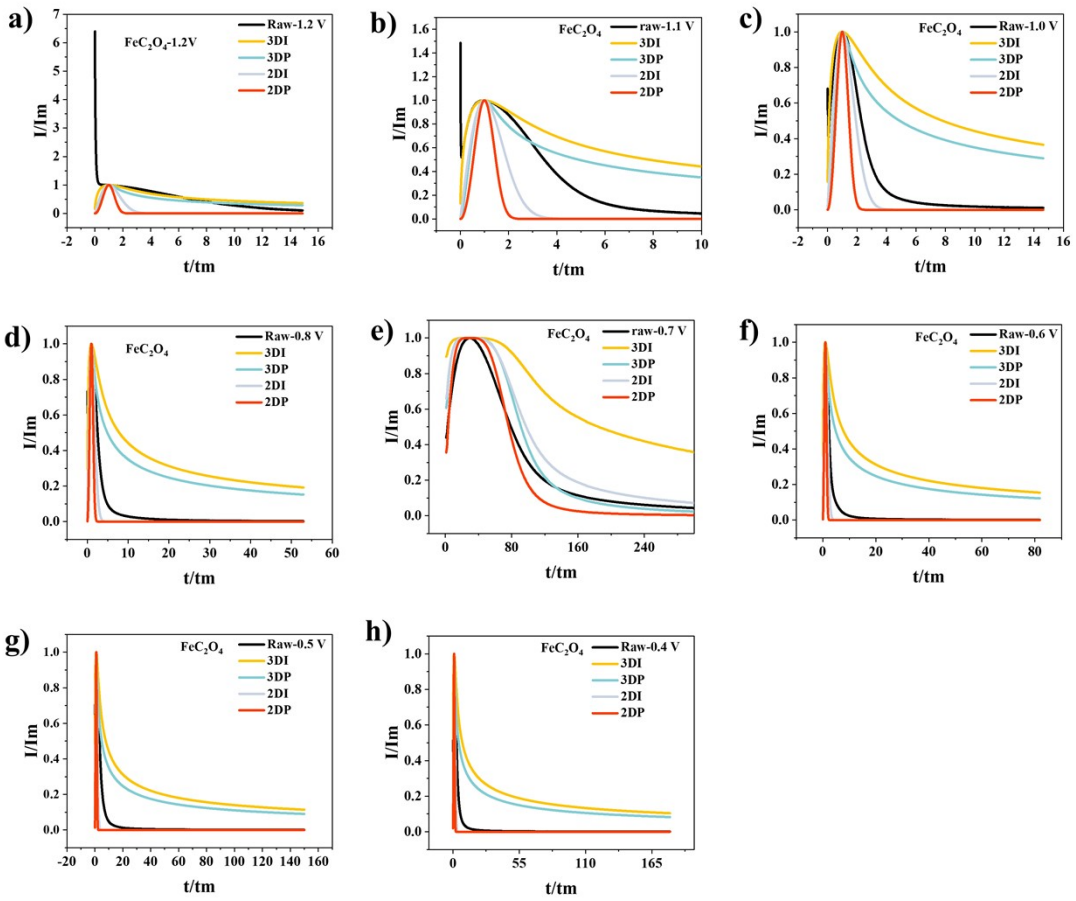

Figure S18. Dimensionless current-time transients compared with 2D and 3D nucleation models for FeC_2O_4 electrodes at different voltages (Vs Li / Li^+). (a) 1.2 V, (b) 1.1 V, (c) 1.0 V, (d) 0.8 V, (e) 0.7 V, (f) 0.6 V, (g) 0.5 V, (h) 0.4 V.

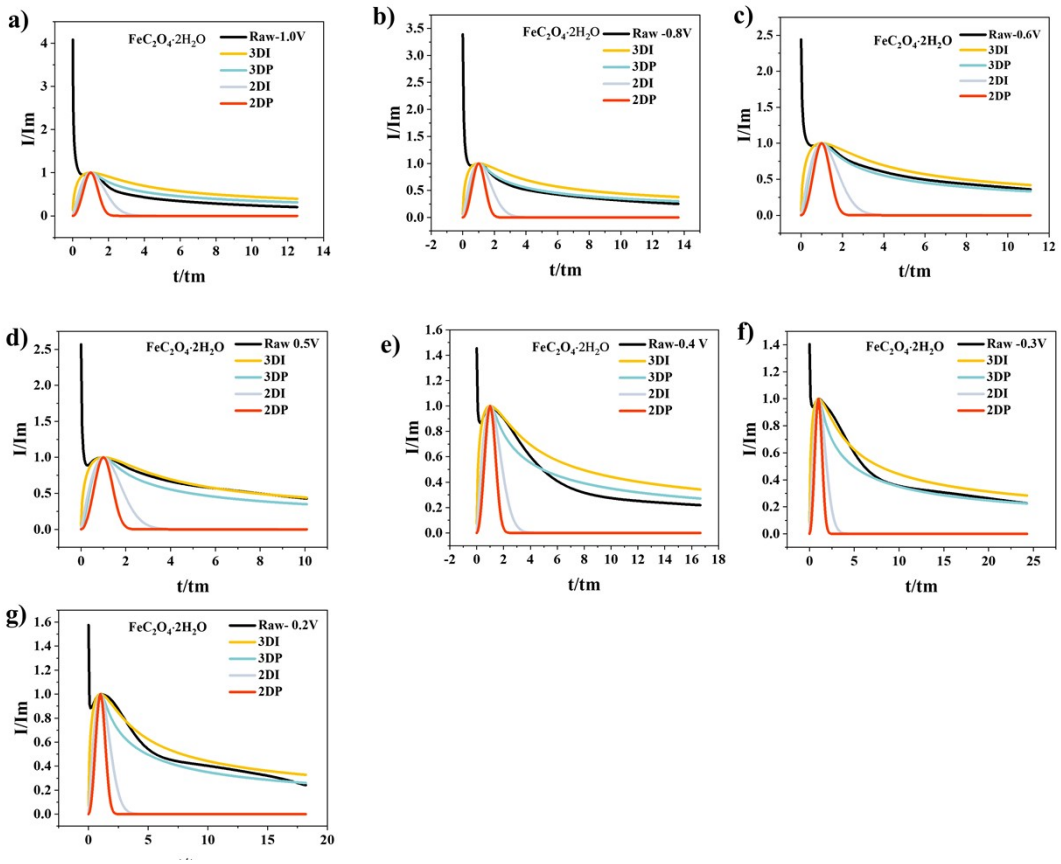

Figure S19. Dimensionless current-time transients compared with 2D and 3D nucleation models for $FeC_2O_4 \cdot 2H_2O$ electrodes at different voltages (Vs Li / Li^+). (a) 1.0 V, (b) 0.8 V, (c) 0.6 V, (d) 0.5 V, (e) 0.4 V, (f) 0.3 V, (g) 0.2 V.

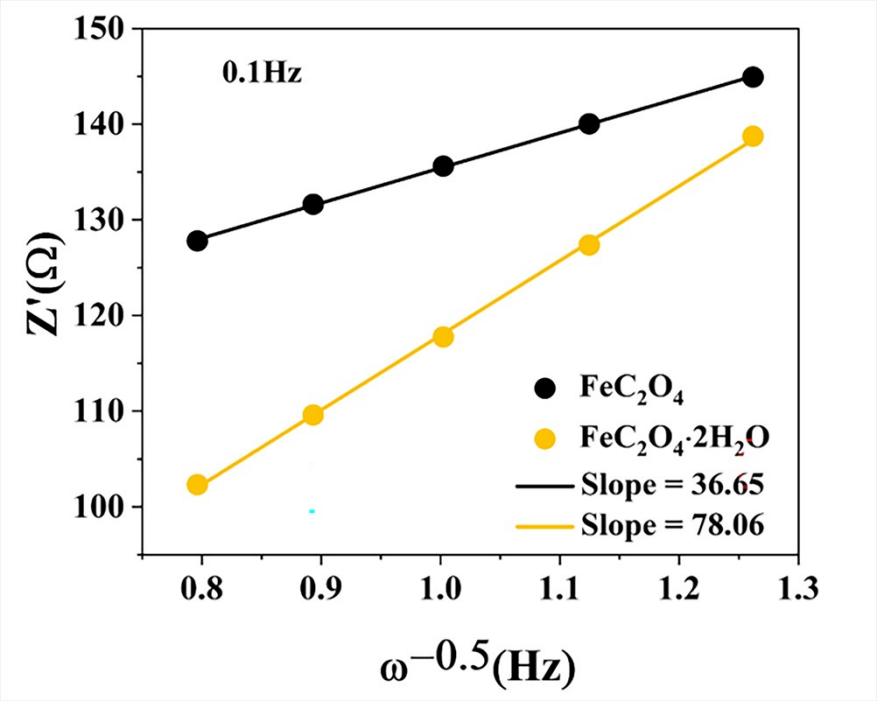

Figure S20. The relationship between Z' and $\omega^{-0.5}$ from Figure 5f after 100 cycles.

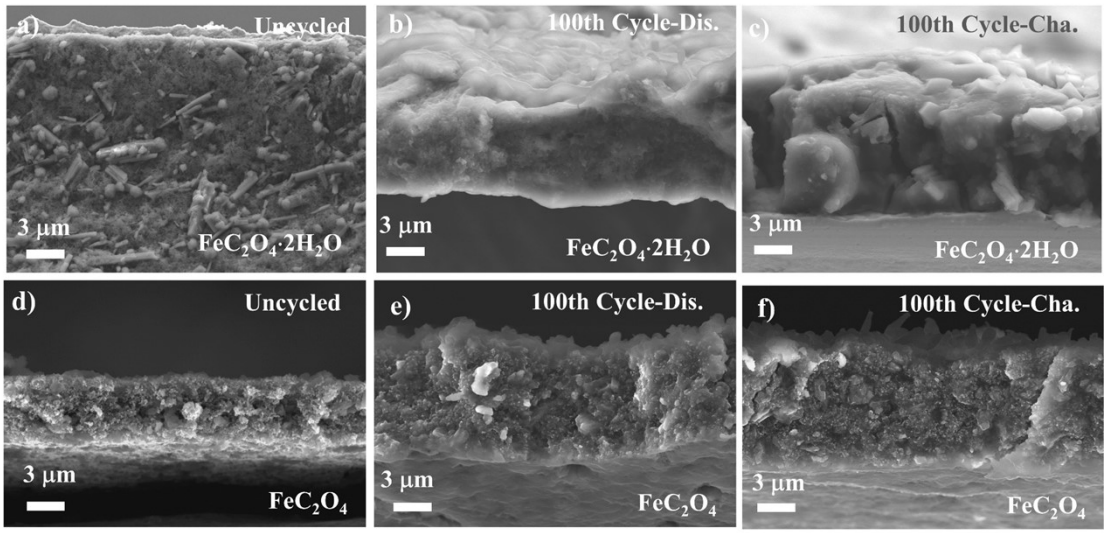

Figure S21. SEM cross-sectional images of the iron oxalate electrodes at different cycles: (a-c) $FeC_2O_4·2H_2O$, (d-f) FeC_2O_4.

Reference

[1] W. Yu, C. Lin, Q. Li, J. Zhang, P. Yang, M. An, A novel strategy to electrodeposit high-quality copper foils using composite additive and pulse superimposed on direct current, Journal of Applied Electrochemistry, 51(3) (2020) 489-501.

[2] Larson, A. C; Dreele, R. B. V. "General Structure Analysis System (GSAS)", Los Alamos National Laboratory Report LAUR 86-748 (1994).

[3] Toby, B. H. EXPGUI, a graphical user interface for GSAS, Journal of Applied Crystallography, 34 (2001) 210-213.

[4] L. Wang, Z. Huang, S. Guo, X. Wu, H. Shen, H. Zhao, G. Jing, Computationally assisted, surface energy-driven synthesis of Mn-doped Co_3O_4 fibers with high percentage of reactive facets and enhanced activity for preferential oxidation of CO in H_2, Journal of Catalysis, 406 (2022) 107-114.

[5] Wan, T. H; Saccoccio, M; Chen, C; Ciucci, F. Influence of the Discretization Methods on the Distribution of Relaxation Times Deconvolution: Implementing Radial Basis Functions with DRT tools. Electrochim Acta. 184 (2015) 483-499.

[6] Y. Wang, Z. Wang, C.-T. Dinh, J. Li, A. Ozden, M. Golam Kibria, A. Seifitokaldani, C.-S. Tan, C.M. Gabardo, M. Luo, H. Zhou, F. Li, Y. Lum, C. McCallum, Y. Xu, M. Liu, A. Proppe, A. Johnston, P. Todorovic, T.-T. Zhuang, D. Sinton, S.O. Kelley, E.H. Sargent, Catalyst synthesis under CO_2 electroreduction favours faceting and promotes renewable fuels electrosynthesis, Nature Catalysis, 3(2) (2019) 98-106.

[7] Z. Zhang, H. Zhao, Z. Du, X. Chang, L. Zhao, X. Du, Z. Li, Y. Teng, J. Fang, K. Świerczek, (101) Plane-Oriented SnS_2 Nanoplates with Carbon Coating: A High-Rate and Cycle-Stable Anode Material for Lithium Ion Batteries, ACS Applied Materials & Interfaces, 9(41) (2017) 35880-35887.

[8] J. Song, L. Wang, G. Shao, M. Shi, Z. Ma, G. Wang, W. Song, S. Liu, C. Wang, Controllable synthesis, morphology evolution and electrochemical properties of $LiFePO_4$ cathode materials for Li-ion batteries, Physical Chemistry Chemical Physics, 16(17) (2014) 7728-7733.

[9] S. Yang, M. Hu, L. Xi, R. Ma, Y. Dong, C.Y. Chung, Solvothermal Synthesis of Monodisperse $LiFePO_4$ Micro Hollow Spheres as High Performance Cathode Material for Lithium Ion Batteries, ACS Applied Materials & Interfaces, 5(18) (2013) 8961-8967.

[10] Y. Liu, J. Wu, W. Zhao, J. Chu, T. Qi, Study on Lithium Insertion in Lepidocrocite and λ-MnO_2 Type TiO_2: A First-Principles Prediction, Chinese Journal of Chemistry 31(10) (2013) 1257-1262.

[11] D. Li, H. Zhao, S. Li, B. Wei, J. Shuai, C. Shi, X. Xi, P. Sun, S. Meng, L. Gu, Z. Ren, X. Chen, Atomic Disorders Induced by Silver and Magnesium Ion Migrations Favor High Thermoelectric Performance in α-MgAgSb-Based Materials, Advanced Functional Materials, 25(41) (2015) 6478-6488.

[12] K. Zhang, Y. Li, Y. Wang, J. Zhao, X. Chen, Y. Dai, Y. Yao, Enhanced electrochemical properties of iron oxalate with more stable Li+ ions diffusion channels by controlling polymorphic structure, Chemical Engineering Journal, 384 (2020).

[13] Y. Fu, C. Peng, D. Zha, J. Zhu, L. Zhang, X. Wang, Surface pore-containing $NiCo_2O_4$ nanobelts with preferred (311) plane supported on reduced graphene oxide: A high-performance anode material for lithium-ion batteries, Electrochimica Acta, 271 (2018) 137-145.

[14] R. Zhang, Q.F. Fu, P. Gao, W. Zhou, H. Liu, C.H. Xu, J.F. Wu, C.J. Tu, J.L. Liu, Transition metal carbonate anodes for Li-ion battery: fundamentals, synthesis and modification, Journal of Energy Chemistry, 70 (2022) 95–120.

[15] Y. X. Yao, J. Wan, N. Yan. Liang, C. Yan, R. Wen, Q. Zhang, Nucleation and Growth Mode of Solid Electrolyte Interphase in Li Ion Batteries, Journal of the American Chemical Society, 145 (2023) 8001-8006.

[16] C. Yan, Li. Li. Jiang, Y.X. Yao, Y. Lu, J.Q. Huang, Q. Zhang. Nucleation and Growth Mechanism of Anion-Derived Solid Electrolyte Interphase in Rechargeable Batteries, Angewandte Chemie International Edition, 60 (2021), 8521–8525.